TITANIQ THERMOBAROMETERY OF FABRIC DEVELOPMENT IN THE STRAFFORD DOME, VERMONT: LINKING MICROSTRUCTURES TO OROGENIC PROCESSES

A Progress Report Presented

by

Kyle Thomas Ashley

to

The Faculty of the Geology Department

of

The University of Vermont

November 1, 2010

Accepted by the Faculty of the Geology Department, the University of Vermont, in partial fulfillment of the requirements for the degree of Master of Science in specializing in Geology.

The following members of the Thesis Committee have read and approved this document before it was circulated to the faculty:

_____ Laura E. Webb	**Advisor**
_____ Arne Bomblies	**Committee Chair**
_____ Keith A. Klepeis	**Committee Member**
_____ Frank S. Spear	**Committee Member**
_____ Robert L. Badger	**Committee Member**

Date Accepted: _____

Introduction

Investigation into trace element budgets in quartz has resulted in the establishment (and refinement) of the Ti-in-quartz ("TitaniQ") thermobarometer with precision of temperature estimates on the order of ± 5°C (2σ; if pressure is well constrained; Wark and Watson, 2006; Thomas *et al.*, 2010). Because quartz is nearly ubiquitous in rocks of the continental crust, TitaniQ provides new opportunities for accurate thermobarometry and constraining pressure-temperature-time-deformation (*P-T-t-D*) histories of tectonites. This project is currently identifying the process to correctly use TitaniQ thermobarometry in *P-T-t-D* studies – something that has not yet been established and will be the focus of a peer-review publication. The findings will be evaluated to determine the usefulness of TitaniQ in tectonic studies.

Trace element uptake into the quartz lattice has been well established through previous studies (e.g. Weil, 1984, 1993; Götze *et al.*, 2004). Quartz is regarded to only incorporate a relatively small amount of superfluous elements into its lattice because of the small size and structure of the Si^{4+} ion. Incorporation into the quartz lattice is achieved through substitution for Si (Al, Ti, Ge) and interstitial filling (Li, Na, K; Götze *et al.*, 2004; Berry *et al.*, 2007). Ti isomorphically and isoelectronically substitutes for Si in the quartz lattice due to the tetravalent nature of both Ti and Si cations; substitution can be achieved without charge balancing through coupled substitution of other elements (Ostapenko *et al.*, 1987; Farges *et al.*, 1996a, 1996b; Farges, 1997; Farges *et al.*, 1997; Götze *et al.*, 2004; Wark and Watson, 2006; Ostapenko *et al.*, 2007). Solubility is dependent on $a_{TiO_2}^{qtz}$, which is typically fixed when quartz is recrystallized in the presence of TiO_2 systems (e.g. rutile a_{TiO_2}= 1; titanite a_{TiO_2} = 0.5; Wark and Watson, 2006). In phases where TiO_2 is not an essential stoichiometric component, TiO_2 activity may be calculated (a_{TiO_2} is ~1 for metapelites and ≥0.8 for amphibolites-facies felsic gneisses; Ghent and Stout, 1984; Wark and Watson, 2006). For *P-T* determination, an independent estimate of pressure

or temperature is required, or both can be obtained through simultaneous use with another thermobarometer (e.g. Zr-in-rutile, Zr-in-sphene, and Ti-in-zircon; Hayden *et al.*, 2006; Watson *et al.*, 2006; Thomas *et al.*, 2010).

Previous studies on cathodoluminescence (CL) imaging of quartz have shown that CL intensity at 415 nm (blue) wavelength is proportional to Ti concentrations due to the element's CL emission properties (Wark and Spear, 2005; Rusk *et al.*, 2006, 2008; Spear and Wark, 2009), which is useful in distribution analysis of Ti in a single crystal (i.e. zoning) or comparing neighboring crystals. Calculated characteristic transport distances in which Ti diffuses in quartz are: 2 μm and 5 μm in 1.0 and 10 Ma, respectively (at 500°C; Cherniak *et al.*, 2004, 2007). The implications of this are that either high temperatures, small grain sizes or long times are required to have cores record peak *P-T* conditions for equilibration during prograde metamorphism (for quartz that is not deforming or the product of a reaction).

The abundance and stability of quartz under various metamorphic conditions makes this method practical. Analyses are being conducted on phyllitic/schistose and gneissic samples from the Strafford Dome, east-central Vermont (Figure 1). The Strafford Dome provides an exceptional field area because traverses across the dome can be completed through a gradient in metamorphic conditions from biotite to peak kyanite/staurolite grade zones and an extensive existing petrologic framework has been established for the region (Menard, 1991; Menard and Spear, 1994). Fabrics preserved in samples from the various zones record fabric development during prograde, peak and retrograde metamorphism associated with the Acadian Orogeny (397—350 Ma; Spear and Harrison, 1989). Quartz recrystallization in different microstructural settings, such as inclusion trails in porphyroblasts and pressure shadows, is examined and permits establishment of deformational temporal and thermal sequences. Deformation is attributed to two nappe emplacement events, with later space or kink banding occurring (Table 1;

Figure 2). Temperature is inferred through [Ti] measurements with pressure constraints (through use of another theromobarometer or garnet composition analysis) and will be elucidated in terms of microstructural evolution. The results will be interpreted in the context of *P-T* paths and regional tectonic evolution.

Work Conducted to Date

The project initiated during the summer of 2009 with sixteen samples collected throughout the Strafford Dome (Figure 1). An additional eight non-oriented samples of the T. Menard thesis collection were provided by Frank Spear at Rensselaer Polytechnic Institute (RPI) that contain structures pertinent to this project. My efforts focused on collection of samples along a traverse across the metamorphic isograds of the dome from garnet to staurolite/kyanite. The biotite zone was excluded due to decreased metamorphic conditions that would result in lower [Ti] measurements. Thin section billets were cut oriented normal to foliation and parallel to lineation, or parallel to the down-dip direction in the absence of lineation. A second billet was prepared normal to foliation and orthogonal to the first billet. In all, twenty nine oriented and nine non-oriented thin sections were prepared to a microprobe quality polish.

Petrographic and microstructural analyses were conducted on the thin sections (Table 2; Table 3) with target areas selected for electron microprobe and cathodoluminescence (CL) analyses at RPI. CL imaging with a 415 nm (blue) exhibits Ti-distribution in quartz with influences by strain in the crystal lattice (Figure 3). Back-scattered electron images (BSEs) were collected of target areas and elemental X-ray maps of garnet porphyroblasts were obtained (Figure 4). Chemical zoning in garnet can be observed with the X-ray maps, and spot analyses were performed to calibrate the maps for quantitative analysis. Chemical profiles of the porphyroblasts were constructed to make interpretations on metamorphic

conditions during garnet growth, and thus while quartz was being encapsulated. Spot analyses were conducted on quartz crystals with the electron microprobe (Table 4), although [Ti] were nearing detection limits and were not reliable and accurate enough for this study.

X-ray mapping of a snowball garnet revealed an increase in Mn (X_{sps}), a decrease in Mg (X_{pyp}), and constant Fe (X_{alm}) with growth. Ca only increases in regions along the rim (Table 5; Figure 4; Figure 5). This zoning suggests the garnet grew with increasing pressures and slightly decreasing temperatures. Knowing the thermobarometric conditions during garnet growth constrains the peak conditions for quartz before/during being included (Figure 6). If quartz recrystallized during garnet growth, we would expect it to record *P*-*T* conditions similar to that of the garnet.

Regions of interest were selected from the thin sections and drilled out for further analysis. A microdrill was used to remove the target areas (typically >1 mm), which were placed on double-sided sticky tape and placed within a one inch round. Epoxy was poured into the round, originally under vacuum to evacuate any bubbles, and left to cure overnight. This resulted in a "puck" that can be used in both the electron microprobe and the SIMS. By drilling the samples, time is saved during analysis because the area being searched corresponding to the CL images collected is significantly diminished relative to the thin section.

Preliminary spot analyses were conducted using the SIMS at the Woods Hole Oceanographic Institute (WHOI; Table 6). The samples were gold coated to eliminate charging across the surface of the puck. Several analyses were taken but the trip ended prematurely due to a problem with focusing the oxygen beam causing the analysis to progressively take longer with larger errors associated (e.g. Figure 7).

Quartz inclusions in garnet porphyroblasts typically have brighter rims (typically <5 μm) when observed in CL and is attributed to diffusion of Ti from the garnet. Most quartz inclusions contain bright

bands in CL correlating to planar defects. Preliminary analysis shows [Ti] in quartz near the core of the snowball garnet to be 10.5–13.0 ppm, ≥12.5 ppm near the garnet rim, 8.0–11.0 ppm in the matrix grains, and ~17.0 ppm near foam texture triple junctions. Rotated garnets locally contain inclusions that appear brecciated in CL images (kyanite/staurolite zone; e.g. Figure 3k). In samples where the dominant foliation is a bedding parallel schistosity (S_1), ribbon quartz grains and subgrains are present (kyanite/staurolite zone; Figure 8). The subgrains typically have sharp, dark rims with brighter mantles. Some grains contain dark cores near the center. Larger ribbon grains still have the dark rims, but are more homogeneous internally. Crenulated matrix quartz (S_2), where present, contains bright rims with darker mantles (garnet zone). In some cases, bright cores are found in the center of these grains. Quartz veins that post-date the foliation within the samples are typically homogeneous, with only minor patchy bright spots present and no observable zoning. Deformed quartz veins in some samples contain ribbon quartz and preserve subgrain rotation recrystallization microstructures (kyanite/staurolite zone). The ribbon quartz is very patchy where subgrains are beginning to consume the ribbon grain.

X-ray powder diffraction (XRPD) is currently being done on samples with varying known [Ti]. It is hypothesized that lattice parameters of the quartz lattice may relate to Ti substituting for Si. If there is a correlation between the two, then XRD analysis could be a potential tool in thermobarometry studies and would be significantly cheaper (and faster) to collect data from samples of interest. Although due to the inability to precisely target a region of a grain like you could for SIMS, LA-ICP-MS, electron microprobe, etc., quartz grains analyzed would need to be unzoned. This study is a project in partial fulfillment of an XRD course at the University of Vermont and is not critical for the thesis.

Hypothesis and Preliminary Interpretations

Initial results from analyzing spatial variation in chemistry of garnet have shown the rotated garnet (TM783) grew during increasing pressure and slightly decreasing temperature, most likely

associated with nappe emplacement. Some garnets from sample TM455 grew quickly (unzoned), although may contain a secondary growth on the rim; determined from significant chemical differences and a sharp contact with the rest of the grain (Figure 9).

Sample 09SD08A contains garnet porphyroblasts with included S_1 cleavage (Figure 10). Garnet growth was most likely inter-kinematic (post-D_1 and pre-D_2, or $D_1<P<D_2$). Pressure shadows form on the porphyroblasts as a result of inhomogeneous strain in the sample due to the rigidity of the porphyroblasts relative to the groundmass. The quartz vein in this sample post-dates deformation.

Schistosities from S_0 to S_3 are visible in sample TM623 (Figure 11). Quartz veins in this sample post-date deformation. Garnet porphyroblasts are either inter- or syn-tectonic ($D_2<P<D_3$ or $D_3 \supset P$) with crenulated inclusion trails.

TM455 contains two stages of garnet growth ($D_1<P<D_2$ and $D_3 \supset P$). Quartz veins in this sample predate deformation, with dynamic recrystallization being the dominant mechanism in the domains. Ribbons are visible at the hinges of the folded veins where strain is minimal, although subgrains completely consume these ribbons on the limbs.

Kyanite growth (sample TM783) predated garnet growth because it is being partically included by the garnet. This implies any quartz-producing reactions for kyanite growth would predate garnet growth and may have quartz included from this reaction. The rotated garnet infers a syn-deformational growth ($D_3 \supset P$) and counter clock-wise rotation sense in the sample (Figure 3). The inclusions of quartz that appear brecciated may be indicative of previous faulting before being encapsulated (Figure 3k). This, however, may complicate TitaniQ thermobarometry measurements because the use of this method is assuming a system in equilibrium. Many of the samples have polygonized matrix quartz with foam textures (120° triple junctions between grain boundaries), suggesting periods of elevated temperatures and pressure after deformation.

Work Remaining

Additional collected samples were prepared and sent out to be made into thin sections. Once they arrive, mineralogical, petrographic, petrologic and microstructural analysis of the thin sections will be conducted. CL images will be taken for regions of interest with targets being microdrilled and additional pucks prepared for SIMS analysis. Additional trips to the ion probe at WHOI will be made to collect additional quantitative data for the samples (Table 7). Further garnet analysis (compositional profiles and X-ray mapping) will be conducted to allow for better constraints on the microstructural and thermobarometric context of quartz in the samples; THERMOCALC (or Program GIBBS) will be used to create pseudosections to accomplish this goal.

After the analyses are completed, calculations for *P-T* conditions of quartz recrystallization will be made. There will be an integration of observations, structural data, microstructural contexts of quartz, petrological interpretations, qualitative and quantitative data. This will allow for the construction of *P-T-t-D* histories for the rock. A final assessment of the validity of TitaniQ in determining these histories in tectonites will be made, comparing our results with those of previous studies. A timeline for the remaining work to be completed can be found in Table 7.

References

Berry, A. J., Walker, A. M., Hermann, J., HStC O'Neill, Foran, G. F. & Gale, J. D., 2007. Titanium substitution in forsterite. *Chemical Geology*, **242**, 176—186.

Cherniak, D. J., Wark, D. A. & Watson, E. B., 2004. Ti diffusion in quartz: preliminary findings. *American Geophysical Union*, Spring Meeting, abstract #V43C-10.

Cherniak, D. J., Watson, E. B. & Wark, D. A., 2007. Ti diffusion in quartz. *Chemical Geology*, **236**, 65—74.

Doll, C. G., 1944. A preliminary report on the geology of the Strafford Quadrangle, Vermont. *Vermont Geological Survey* (24th report of the State Geologist), 14—28.

Doll, C. G., Cady, W. M., Thompson, J. B., Jr. & Billings, M. P., 1961. *Centennial Geologic Map of Vermont*, Vermont Geological Survey, Montpelier, VT.

Farges, F., 1997. Coordination of Ti^{4+} in silicate glasses: A high-resolution XANES spectroscopy study of the Ti K edge. *American Mineralogist*, **82**, 36—43.

Farges, F., Brown, G. E. Jr. & Rehr, J. J., 1996a. Coordination chemistry of Ti(IV) in silicate glasses and melts: I. XAFS study of titanium coordination in oxide compounds. *Geochemica et Cosmochimica Acta*, **60**, 3,023—3,038.

Farges, F., Brown, G. E. Jr. & Rehr, J. J., 1996b. Coordination chemistry of Ti(IV) in silicate glasses and melts: II. Glasses at ambient temperature and pressure. *Geochemica et Cosmochimica Acta*, **60**, 3,039—3,053.

Farges, F., Brown,, G. E. Jr. & Rehr, J. J., 1997. Ti K-edge XANES studies of Ti coordination and disorder in model compounds: Comparison between theory and experiment. *Physics Review B*, **56**, 1,809—1819.

Fisher, G. W., & Karabinos, P., 1980. Stratigraphic sequence of the Gile Mountain and Waits River Formations near Royalton, Vermont. *Geological Society of America Bulletin*, **91**, 282—286.

Ghent, E. D. & Stout, M. Z., 1984. TiO_2 activity in metamorphosed pelitic and basic rocks: Principles and applications to metamorphism in southeastern Canadian Cordillera. *Contributions to Mineralogy and Petrology*, **86**, 248—255.

Götze, J., Plötze, M., Graupner, T., Hallbauer, D. K. & Bray, C. J., 2004. Trace element incorporation into quartz: A combined study by ICP-MS, electron spin resonance, cathodoluminescence, capillary ion analysis, and gas chromatography. *Geochimica et Cosmochimica Acta*, **68**(18), 3,741—3,759.

Hayden, L. A., Watson, E. B. & Wark, D. A., 2006. A thermobarometer for sphene. *Goldschmidt conference abstract*.

Holdaway, M. J., 1971. Stability of andalusite and the aluminum silicate phase diagram. *American Journal of Science*, **271**, 97—131.

Kretz, R., 1983. Symbols for rock-forming minerals. *American Mineralogist*, **68**, 277—279.

Menard, T., 1991. *Metamorphism of calcic pelitic schists, Strafford Dome, Vermont*. Unpublished PhD Thesis, Rensselaer Polytechnic Institute.

Menard, T. & Spear, F. S., 1994. Metamorphic *P-T* paths from calcic pelitic schists from the Strafford Dome, Vermont, USA. *Journal of Metamorphic Geology*, **12**, 811—826.

Ostapenko, G. T., Gamarnik, M. Y., Gorogtskaya, L. I., Kuznetsov, G. V., Tarashchan, A. N. & Timoskkova, L. P., 1987. Isomorphism of titanium substitution for silicon in quartz: Experimental data. *Mineral Zh*, **9**, 30—40.

Ostapenko, G. T., Tarashchan, A. N. & Mitsyuk, B. M., 2007. Rutile-quartz geothermobarometer. *Geochemistry International*, **45**, 506—508.

Passchier, C. W., & Trouw, R. A. J., 2005. *Microtectonics*. Springer, Federal Republic of Germany (DEU), Berlin.

Rusk, B. G., Lowers, H. A. & Reed, M. H., 2008. Trace elements in hydrothermal quartz: Relationships to cathodoluminescent textures and insights into vein formation. *Geology*, **36**(7), 547—550.

Rusk, B. G., Reed, M. H., Dilles, J. H. & Kent, A. J. R., 2006. Intensity of quartz cathodoluminescence and trace-element content in quartz from the porphyry copper deposit at Butte, Montana. *American Mineralogist*, **91**, 11,300—1,312.

Spear, F. S. & Harrison, T. M., 1989. Geochronologic studies in central New England I: Evidence for pre-Acadian metamorphism in eastern Vermont. *Geology*, **17**, 181—184.

Spear, F. S., Kohn, M. J., Cheney, J. T. & Florence, F., 2002. Metamorphic, thermal, and tectonic evolution of Central New England. *Journal of Petrology*, **43**(11), 2,097—2,120.

Spear, F. S., Kohn, M. J., Florence, F. P., & Menard, T., 1990. A model for garnet and plagioclase growth in pelitic schists: Implications for thermobarometery and *P-T* path determinations. *Journal of Metamorphic Geology*, **8**(6), 683—696.

Spear, F. S. & Wark, D. A., 2009. Cathodoluminescence imaging and titanium thermometry in metamorphic quartz. *Journal of Metamorphic Geology*, **27**, 187—205.

Thomas, J. B., Watson, E. B., Shemella, P. T., Nayak, S. K. & Lanzirotti, A., 2010. The effect of pressure on Ti-in-quartz solubility: the TitaniQ thermobarometer. *Contributions to Mineralogy and Petrology* (in press). doi: 10.1007/s00410-010-0505-3

Wark, D. A. & Spear, F. S., 2005. Titanium in quartz: Cathodoluminescence and thermometry. *Geochemica et Cosmochimica Acta Supplement*, **69**, A592.

Wark, D. A. & Watson, E. B., 2006. TitaniQ: A titanium-in-quartz geothermometer. *Contributions to Mineralogy and Petrology*, **152**, 743—754.

Watson, D. S., Wark, D. A. & Thomas, J. B., 2006. Crystallization thermometers for zircon and rutile. *Contributions to Mineralogy and Petrology*, **151**, 413—433.

Weil, J. A., 1984. A review of electron spin spectroscopy and its application to the study of paramagnetic defects in crystalline quartz. *Physics and Chemistry of Minerals*, **10**, 149—165.

Weil, J. A., 1993. A review of the EPR spectroscopy of the point defects in α-quartz: The decade 1982-1992. In: Helms, C. R., and Deal, B. R. (eds), *Physics and chemistry of SiO_2 and the Si-SiO_2 Interface 2*. Plenum Press, New York, 131—144.

White, W. S. & Eric, J. H., 1944. Preliminary report on the geology of the Orange County copper district, Vermont. *United States Geological Survey Open-File Report*.

White, W. S. & Jahns, R. H., 1950. Structure of central and east-central Vermont. *Journal of Geology*, **58**, 179—220.

Woodland, B. G., 1977. Structural analysis of the Silurian-Devonian rocks of the Royalton area, Vermont. *Geological Society of America Bulletin*, **88**, 1,111—1,123.

Table 1. *Deformation and Metamorphism of the Strafford Dome*

Deformation Event†		Structure	S_x	M/M Stage	Minerals	Notes
D_1	Early folding	Rare F_1 folds; slaty cleavage	S_1	M_1	Muscovite + biotite ± ilmenite	*P-T* remained constant for extended period
D_2	Nappe emplacement	Crenulation cleavage; large recumbent folds	S_2	M_2	Biotite + muscovite ± plagioclase ± tourmaline + garnet	
D_3	Nappe emplacement	Doming of S_2; local kink banding	-	M_3	Kyanite + staurolite + garnet + plagioclase + biotite	Overgrows S_1 and S_2 during doming.
Post-D_3	-	-	-	M_4	Chlorite + K-spar ± biotite ± calcite ± sericite	Retrograde metamorphism; replaces previous mineral assemblage

† Initial metamorphism occurred in response to the Middle Devonian Acadian Orogeny (Menard and Spear, 1994). Deformation, structures and metamorphic paragenesis are from studies by Doll (1944), White and Eric (1944), Woodland (1977), Fisher and Karabinos (1980), White and Jahns (1950), Menard (1991), Menard and Spear (1994).

Table 2. *Sample Locations and Mineralogy*

	Sample Name	UTM Coordinates†		Mineralogy	Quartz Abundance	Zone	Rock Type
		Northing	Easting				
1	TM485	4852793.0	279297.28	Quartz + feldspar + muscovite ± opaques	abundant	Biotite	Quartz phyllite
2	TM551	4852137.0	282340.78	Quartz + feldspar + biotite + ilmenite ± garnet ± magnetite	domains	Garnet	Quartz-mica phyllite
3	09SD01A	4849833.0	282914.62	Quartz + biotite + feldspar + ilmenite + rutile + zircon	abundant	Garnet	Quartz-mica phyllite/schist
	09SD01B	4849833.0	282914.62	Garnet + biotite + muscovite + feldspar + ilmenite + zircon	none	Garnet	Garnet schist
5	TM623‡	4852176.0	283997.53	Garnet + quartz + feldspar + biotite + muscovite + ilmenite + zircon	domains	Garnet	Garnet schist
6	TM634	4853338.0	286272.22	Garnet + quartz + feldspar + biotite + muscovite + ilmenite + magnetite	abundant	Staurolite	Garnet schist
7	TM521	4851507.5	286526.80	Garnet + quartz + feldspar + biotite + muscovite + rutile ± apatite	abundant	Staurolite	Garnet schist
8	09SD04A	4855901.5	291117.00	Biotite + muscovite + plagioclase + calcite + titanite + opaques + apatite	none	Staurolite	Garnet schist
9	09SD08A‡	4854879.0	293209.30	Garnet + quartz + biotite + feldspar + opaques + rutile	abundant	Staurolite	Garnet schist
	09SD08B	4854879.0	293209.30	Garnet + quartz + biotite + muscovite + feldspar + opaques	abundant	Staurolite	Garnet schist
	09SD08C	4854879.0	293209.30	Garnet + quartz + biotite + feldspar + amphibole + opaques ± rutile	abundant	Staurolite	Garnet schist
	09SD08D	4854879.0	293209.30	Garnet + quartz + albite + K-feldspar + amphibole + titanite + epidote + apatite + chlorite + zircons	abundant	Staurolite	Garnet Gneiss
	TM455‡	4854879.0	293209.30	Garnet + feldspar + muscovite + opaques	domains	Staurolite	Garnet schist
	TM458	4854879.0	293209.30	Garnet + quartz + feldspar + biotite + muscovite ± opaques	domains	Staurolite	Garnet schist
11	09SD06A	4851581.0	298027.90	Garnet + quartz + biotite + muscovite + plagioclase + rutile	inclusions	Staurolite	Garnet schist
12	09SD09A	4855548.0	301658.80	Garnet + quartz + feldspar + amphibole + rutile + magnetite + ilmenite + chlorite + alanite + zircon	abundant	Garnet	Garnet gneiss
13	TM783‡	4865448.0	284272.90	Garnet + quartz + feldspar + biotite + muscovite ±opaques ± zircon	abundant	Staurolite	Garnet-kyanite schist

Note: Numbers in left column (1-13) correspond to sample locations in Figure 1.
†UTM Zone: 43T
‡Samples selected for further analysis.

Table 3. *Microstructure Summary of Samples*

	Sample Name	Qtz. Recryst. Mechanism†	Included Foliation in Grt (S_i)	Grt Growth Relative to Deformation‡	Quartz Occurrence
5	TM623	Static	S_2	$D_2<P<D_3$ or $D_3 \supset P$	Matrix, inclusion, vein (post-tectonic)
9	09SD08A	Static	S_1	$D_1<P<D_2$	Matrix, inclusion, vein (post-tectonic)
9	TM455	SGR	-	$D_1<P<D_2$ and $D_3 \supset P$	Matrix, inclusion, vein (pre-tectonic)
13	TM783	Static	S_3	$D_3 \supset P$	Matrix, inclusion

Note: Numbers in left column correspond to sample locations in Figure 2.

†SGR: subgrain rotation recrystallization

‡⊃ :syn-tectonic

Table 4. *Electron Microprobe Analysis Results (Jan., 2010)*

Sample Name	SiO_2 (wt. %)	Si error (2σ; wt. %)†	TiO_2 (ppm)	Ti error (2σ; ppm)
09SD08A	101.14	0.981	3.7‡	5.6
	101.68	0.985	9.6	5.6
	99.31	0.970	9.8	5.4
	101.59	0.983	8.9	5.6
	100.79	0.979	1.1‡	5.6
	101.37	0.982	2.7‡	5.6
	101.47	0.982	2.0‡	5.6
09SD08D	101.11	0.981	18.1	5.6
	101.41	0.984	2.7‡	5.6
	101.04	0.981	3.8‡	5.6
	102.60	0.991	6.8	5.6
	100.88	0.981	3.6‡	5.6
09SD09A	101.35	0.982	9.6	5.5
	101.66	0.983	-2.2‡	5.6
	101.31	0.983	7.5	5.5
	101.21	0.974	-3.0‡	5.5

†High errors are due to Si Kβ, rather than Si Kα, counting. Si measurement is only for confirmation that the analyzed phase was quartz, and high errors are unimportant.

‡Data below detection limit.

Table 5. *Analysis of garnets (in wt %)*

Sample:	**09SD08A**	**09SD08A**	**TM455**	**TM455**	**TM783**	**TM783**	**TM783**
	rim	core	rim†	core	rim	mantle‡	core
Diameter	2.3 mm		1.5 mm			11.5 mm	
n	5	5	7	5	5	5	5
SiO_2	37.48	37.64	37.43	37.37	37.31	37.36	37.02
TiO_2	0.04	0.14	0.04	0.18	0.07	0.05	0.04
Al_2O_3	21.91	21.57	21.58	20.96	21.63	21.61	21.66
V_2O_3	0.01	0.02	0.01	0.02	0.02	0.02	0.01
Cr_2O_3	0.03	0.02	0.05	0.03	0.03	0.03	0.02
MgO	2.48	1.84	2.60	2.34	2.94	2.67	2.50
CaO	7.81	8.72	6.23	3.72	3.75	3.98	3.84
MnO	1.22	3.66	16.06	18.12	1.95	1.95	3.27
FeO	30.60	27.76	16.82	18.31	33.90	33.93	32.98
ZnO	b.d.	b.d.	b.d.	0.02	0.02	0.01	0.01
Sum	101.58	101.37	100.82	101.07	101.62	101.61	101.35
oxygens	24	24	24	24	24	24	24
Si apfu	5.898	5.941	5.932	5.968	5.912	5.925	5.898
Ti	0.005	0.016	0.005	0.021	0.009	0.006	0.004
Al	4.063	4.011	4.032	3.945	4.040	4.039	4.068
V	0.002	0.003	0.001	0.003	0.003	0.003	0.001
Cr	0.004	0.002	0.007	0.003	0.004	0.003	0.003
Mg	0.582	0.433	0.615	0.558	0.695	0.630	0.593
Ca	1.318	1.474	1.068	0.636	0.636	0.677	0.655
Mn	0.163	0.490	2.156	2.452	0.262	0.262	0.442
Fe^{2+}	4.028	3.664	2.229	2.446	4.493	4.501	4.395
Zn				0.003	0.002	0.001	0.001
Sum	16.063	16.034	16.045	16.035	16.056	16.047	16.060
X_{alm}	0.661	0.604	0.367	0.401	0.737	0.741	0.723
X_{prp}	0.096	0.071	0.101	0.091	0.113	0.104	0.097
X_{sps}	0.027	0.081	0.355	0.402	0.043	0.043	0.073
X_{grs}	0.216	0.243	0.176	0.104	0.104	0.111	0.108
Fe/(Fe+Mg)	0.874	0.894	0.784	0.814	0.866	0.877	0.881

Notes: $X_{alm} = Fe^{2+}$/FMCMnZCrV; X_{prp} = Mg/ FMCMnZCrV; X_{sps} = Mn/ FMCMnZCrV; X_{grs} = Ca/ FMCMnZCrV; FMCMnZCrV = Fe^{2+} + Mg + Ca + Mn + Zn + Cr + V. b.d.—element below the detection limit, not used for mineral formula calculation; apfu—atoms per formula unit.

†From a second generation growth of garnet on the rim of the main garnet.

‡Data collected from region between the rim and the core.

Table 6. *SIMS Analysis on Quartz Inclusions in Garnet (TM783)*

Location in Porphyroblast†	Total Cycles	Cycles Used‡	Ti (ppm)	Ti error (2σ; ppm)
a	40	25	8.00	0.21
a	20	10	17.23	0.52
a	20	10	10.73	0.77
b	30	15	11.58	0.59
b	30	15	10.59	0.28
b	30	15	10.56	0.64
b	30	15	12.63	0.59
c	30	15	12.56	0.70

†Location from CL image shown in Figure x.

‡To account for the surface contamination (analysis of the plateau).

Note: due to oxygen-beam focusing issues, errors are higher than normal and stabalization took longer. Subsequent analysis will be conducted to test the validity of these results.

Table 7. *Remaining Work Timeline*

Fall 2010	• RPI trips for CL and garnet analysis • SIMS analysis of quartz • Write and present progress report • Begin writing paper for peer-review • Submit AGU abstract and present poster at conference (December) • Work on thesis
Winter 2011	• RPI, WHOI trip(s) • Continue work on thesis and manuscript • Integrate analyses and construct interpretations
Spring 2011	• Present at VGS • Finish interpretations and integrating findings • Finish thesis and manuscript • Defend thesis and make corrections • Submitt paper for peer-review

Figure 1. (a) Generalized geologic map of south-eastern Vermont. SD – Strafford Dome; PD – Pomfret Dome; CD – Chester Dome; AD – Athens Dome. Inset map shows location of geologic map, with bands depicting major tectonic belts (modified from Spear *et al.*, 2002): blue band – Eastern Vermont belt; orange band – Merimack belt. Dark rectangle is area shown by the geologic map. Modified from Menard and Spear (1994). Original figure simplified and modified from Doll *et al.* (1961). (b) Metamorphic isograd for same study area shown in (a). P.S. – Plutonic Series. Polymetamorphic areas (denoted by diagonal lines) represent rocks that were previously (Precambrian) metamorphosed to sillimanite zone or higher, but were later (Paleozoic) subjected to lower grade metamorphism. Grades of these rocks are indicated by the color beneath the diagonal lines. Inset illustrates *P-T* paths for the Eastern Vermont tectonic belt (occurring at high pressures, clockwise path) and the Merrimack tectonic belt (occurring at low pressures and high temperatures, counter-clockwise path). Inset *P-T* figure from Spear *et al.* (2002). Numbered points are sample locations, with accompanying sample information in Table 1.

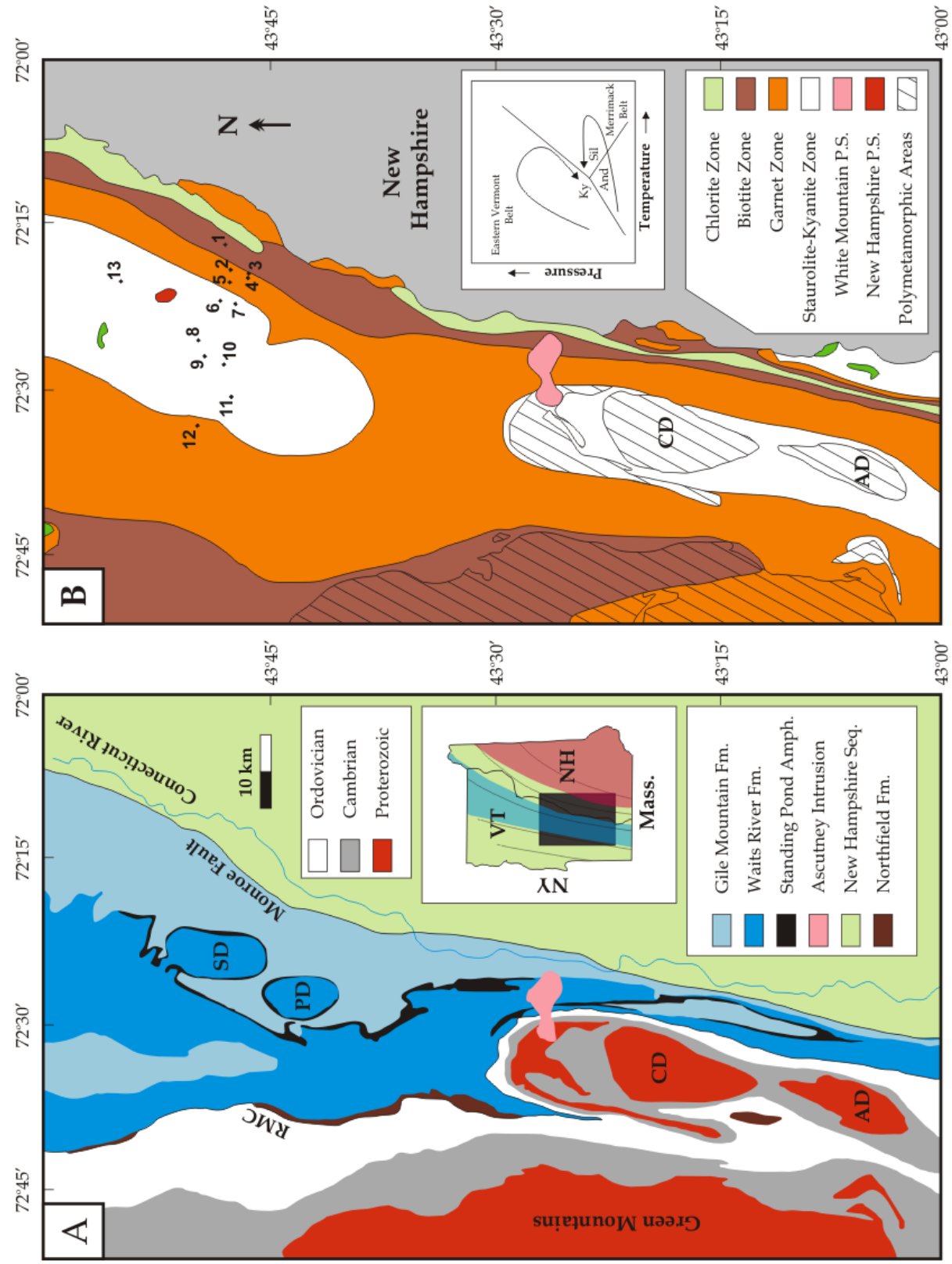
A
B
72°45′
72°30′
72°15′
72°00′
43°45′
43°30′
43°15′
43°00′
Green Mountains
Connecticut River
Monroe Fault
RMC
SD
PD
CD
AD
10 km
Ordovician
Cambrian
Proterozoic
NY
VT
NH
Mass.
Gile Mountain Fm.
Waits River Fm.
Standing Pond Amph.
Ascutney Intrusion
New Hampshire Seq.
Northfield Fm.
N
New Hampshire
Chlorite Zone
Biotite Zone
Garnet Zone
Staurolite-Kyanite Zone
White Mountain P.S.
New Hampshire P.S.
Polymetamorphic Areas
Pressure
Temperature
Eastern Vermont Belt
Merrimack Belt
Ky
And
Sil
.1
.2
.3
4
5.
6.
7.
.8
9.
.10
11.
12.
.13

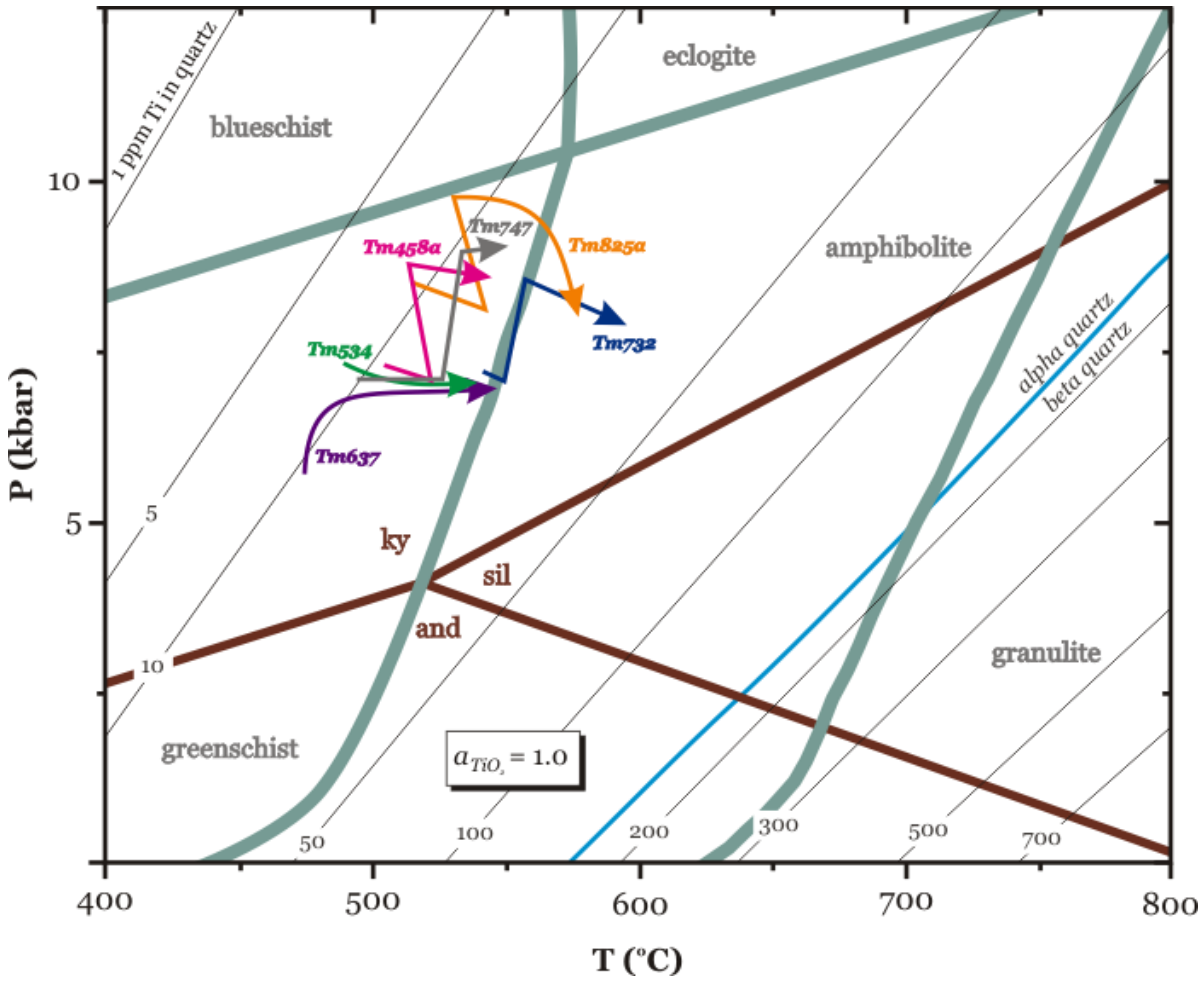

Figure 2. Summary *P-T* paths for select rocks from the Strafford Dome (Menard, 1991; Spear and Menard, 1994; Spear *et al.*, 2002). Ti-in-quartz isopleths (after Thomas *et al.*, *2010*) and Al_2SiO_5 stability fields (after Holdaway, 1971) shown. Isopleths are calibrated to a fixed TiO_2 activity of 1 (rutile present). Modified from Thomas *et al.* (2010).

Figure 3. Cross-polarized photomicrograph of a snowball garnet from sample TM783. Letters “a” through “m” denote locations CL images were captured from and are targets for quantitative analysis. Red boxes are areas where spots analyses have been conducted; green are targets for the next analysis. CL false-colored images of regions a, b and c are presented to the right, with spot analysis results included. Subsequent grey-scale photographs (d-m) are CL images of quartz without any spot analyses conducted on them to date.

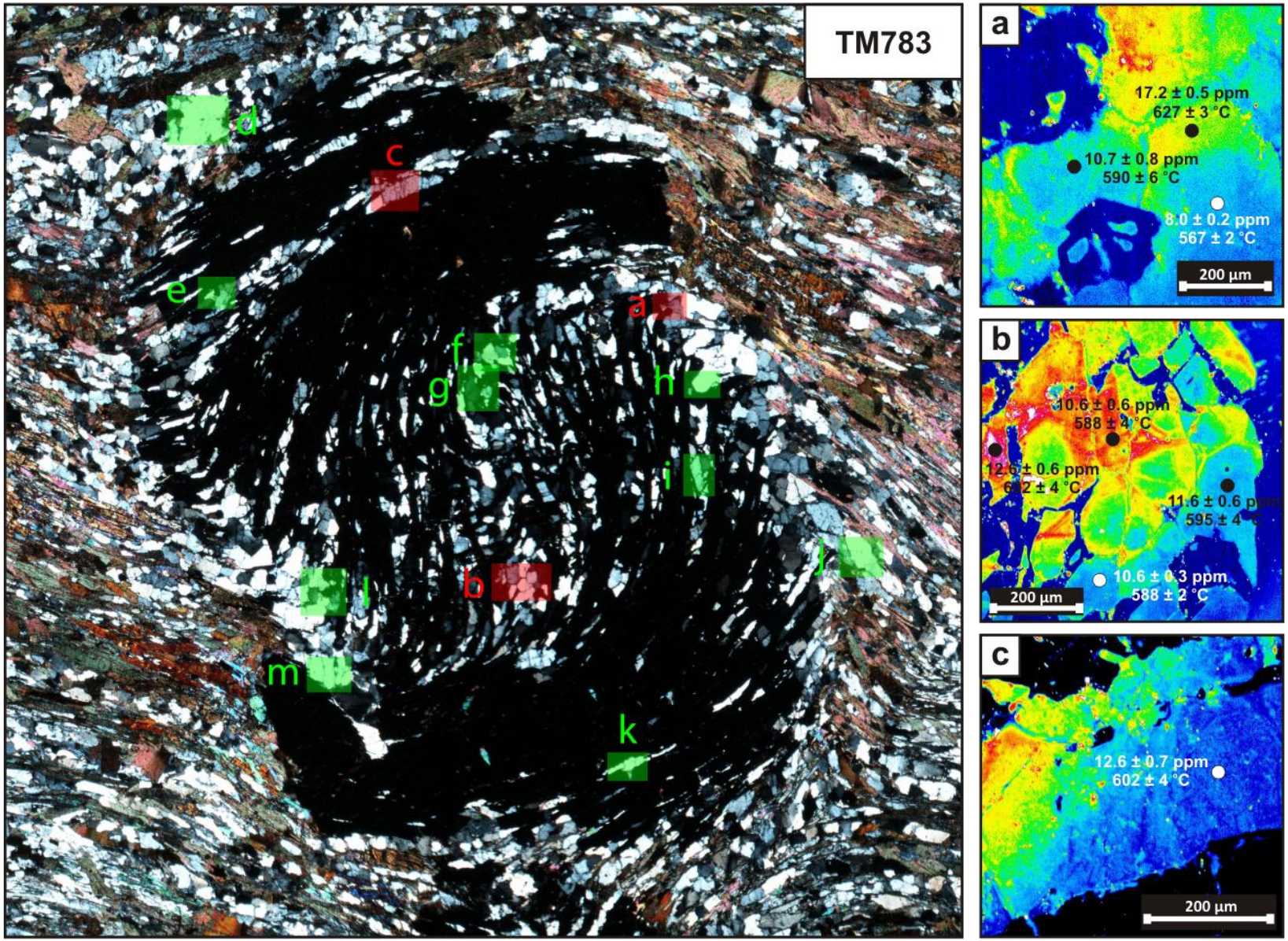
TM783
d
c
e
a
f
g
h
i
j
l
b
m
k
a
17.2 ± 0.5 ppm
627 ± 3 °C
10.7 ± 0.8 ppm
590 ± 6 °C
8.0 ± 0.2 ppm
567 ± 2 °C
200 µm
b
10.6 ± 0.6 ppm
588 ± 4 °C
12.6 ± 0.6 ppm
602 ± 4 °C
11.6 ± 0.6 ppm
595 ± 4 °C
10.6 ± 0.3 ppm
588 ± 2 °C
200 µm
c
12.6 ± 0.7 ppm
602 ± 4 °C
200 µm

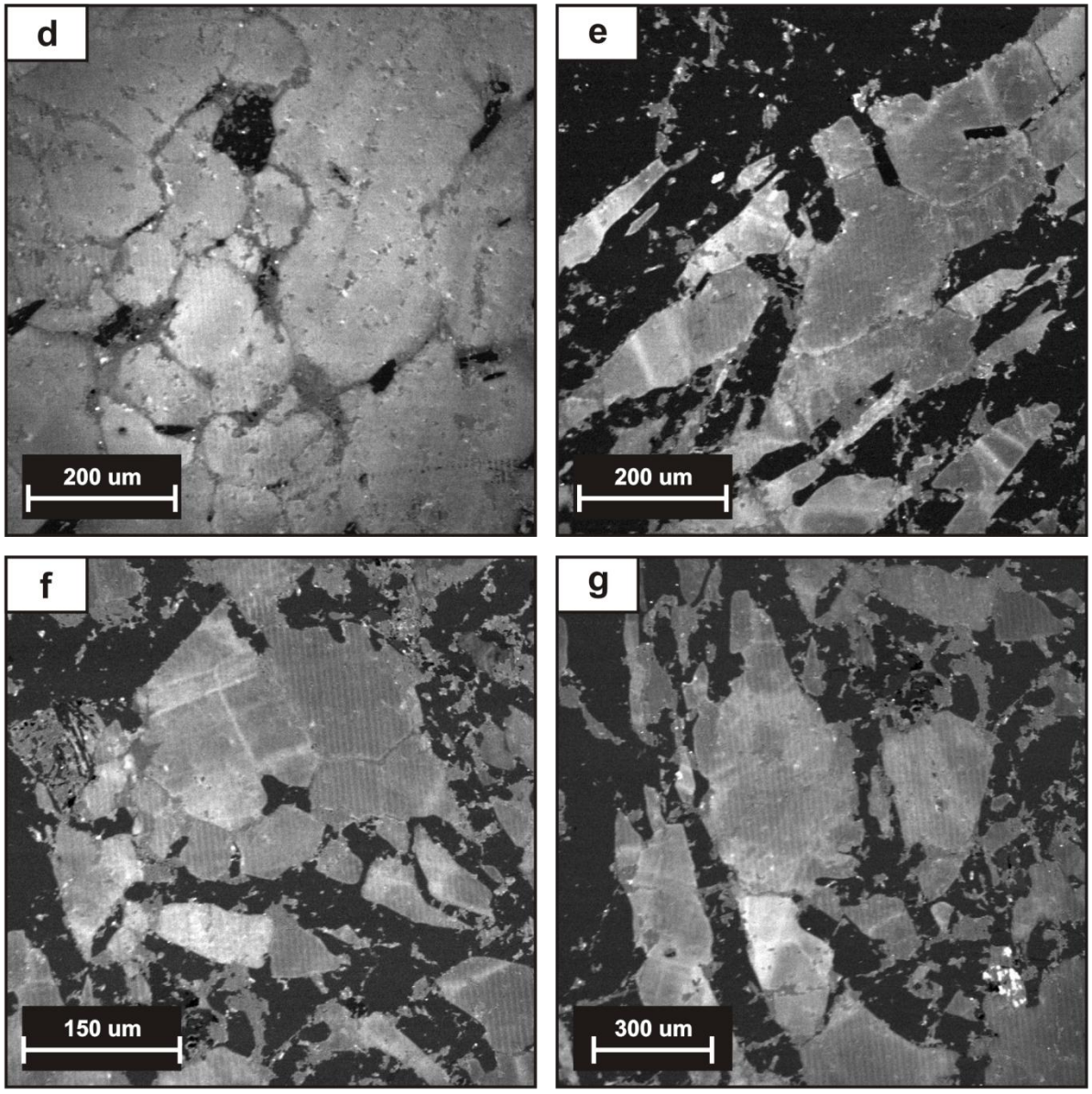
d
200 um
e
200 um
f
150 um
g
300 um

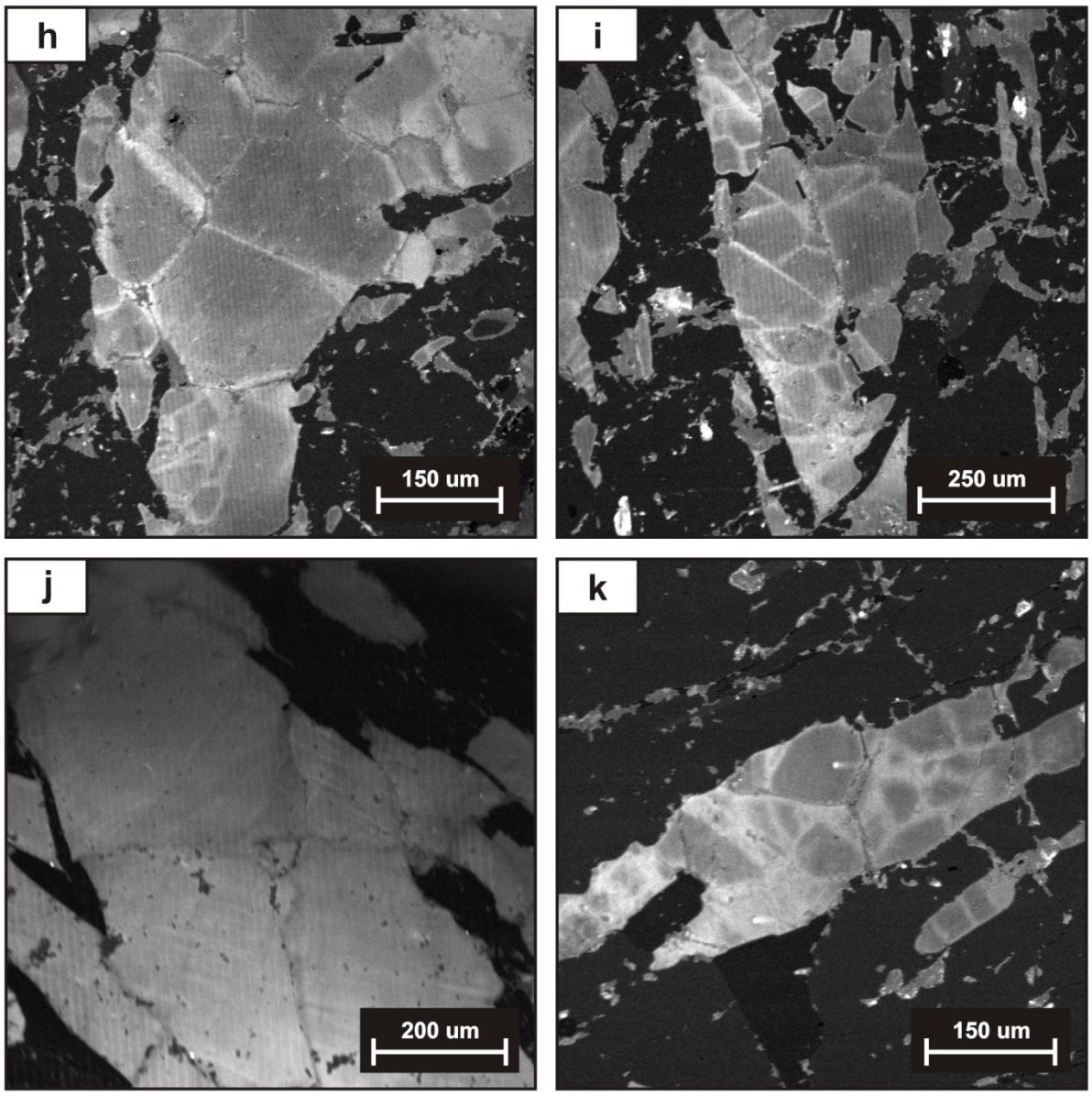
h
150 um
i
250 um
j
200 um
k
150 um

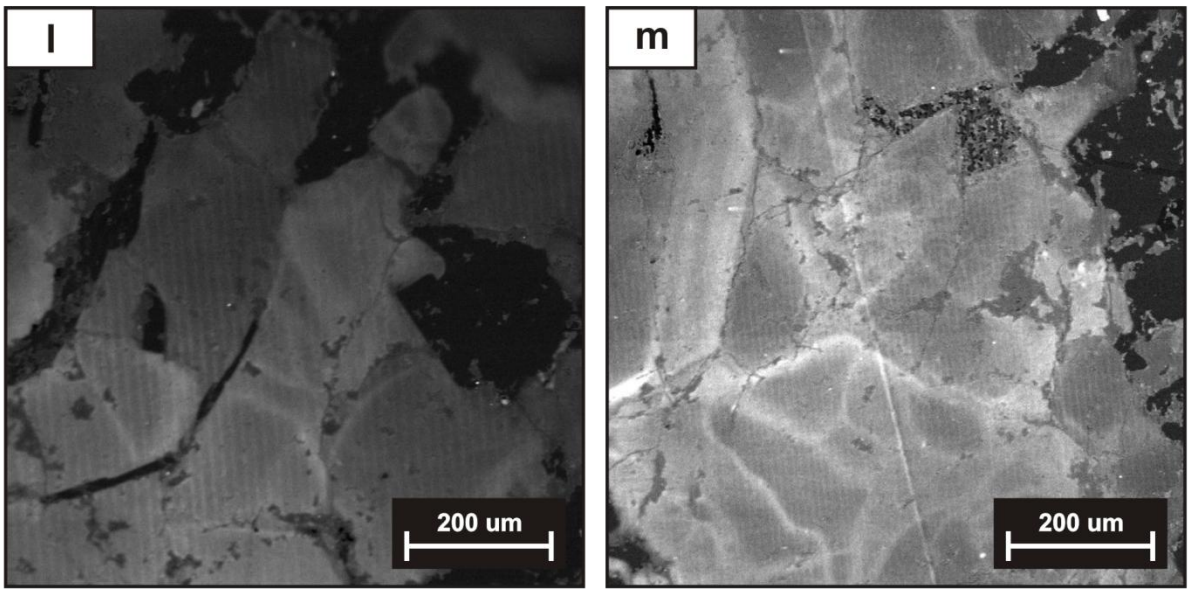
l
200 um
m
200 um

Figure 4. X-ray element maps of snowball garnet from samples TM783. Mn (X_{Sps}) and Mg (X_{Pyp}) are strongly zoned, with X_{Sps} increasing and X_{Pyp} decreasing towards the rim. X_{Alm} (Fe) remains constant throughout the grain. This overall trend is seen in the composition profiles for Mn and Mg (from a—a'), although numerous inclusions of quartz (±biotite, ilmanite, etc.) causes for spikes deviating from the overall trend. This suggests an increase in pressure and a slight decrease in temperature during garnet growth (Spear *et al.*, 1990). There is a slight increase in X_{Ca} on the rim in select areas that may be attributed to re-absorption of Ca into the garnet. X_{Al} and X_{Ti} are constant throughout the grain.

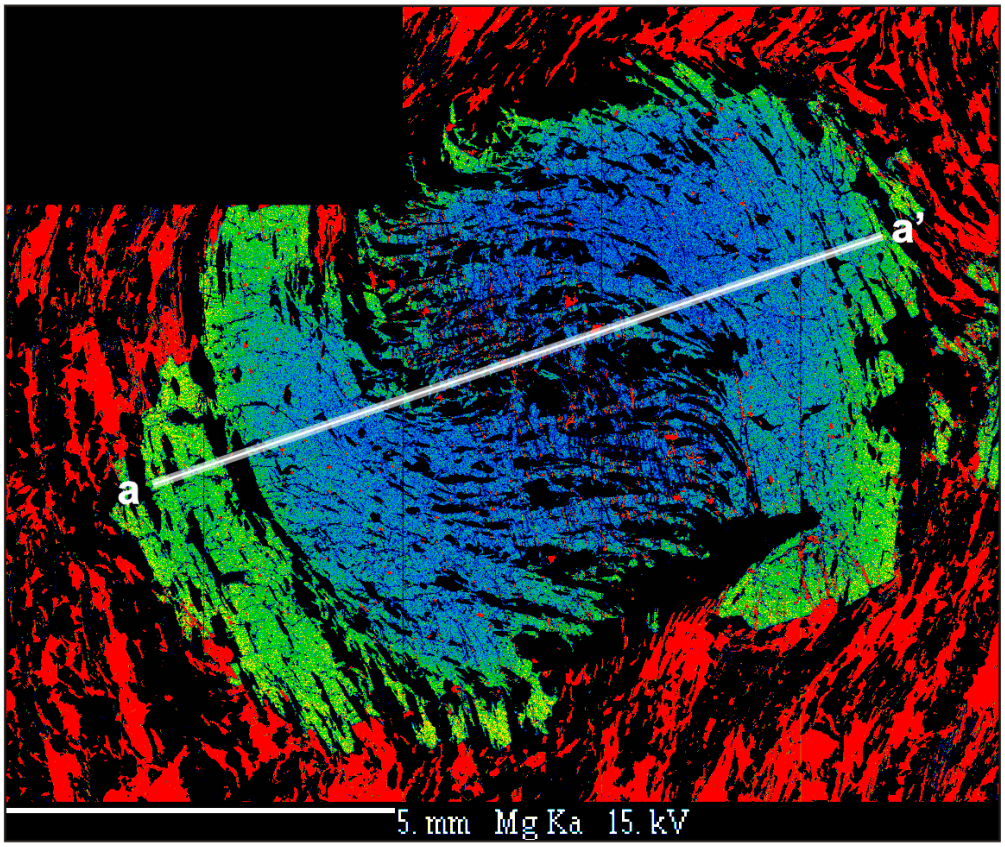
a'
a
5. mm Mg Ka 15. kV

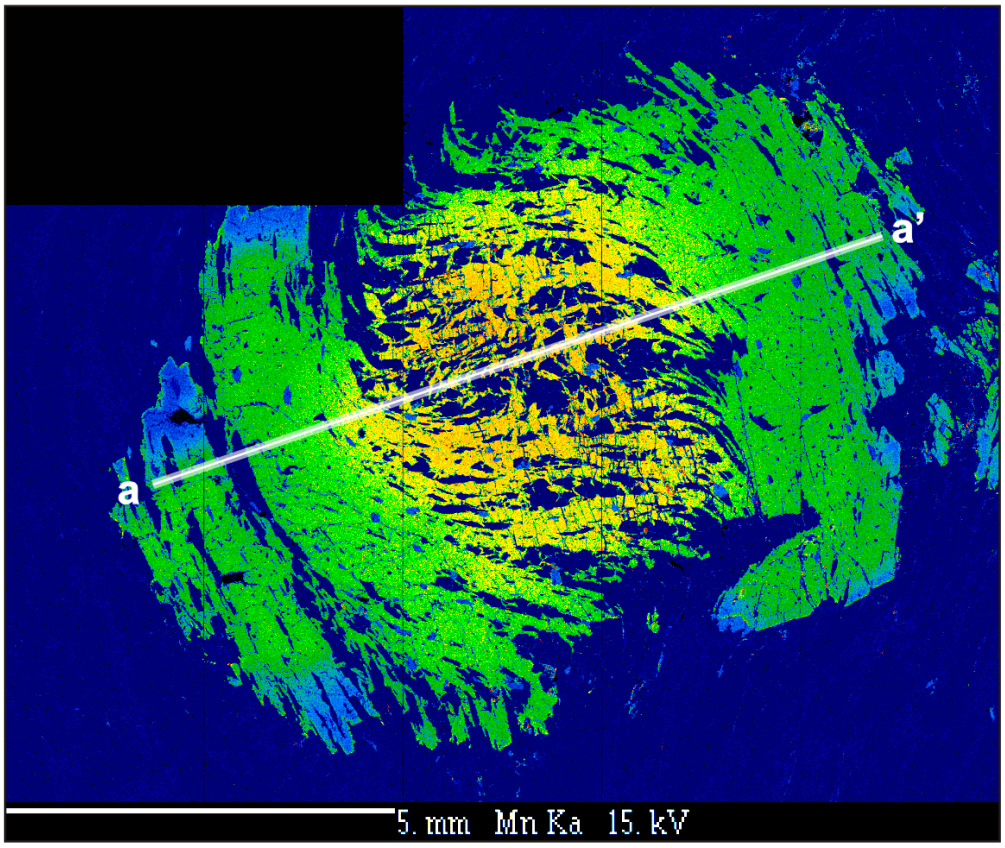
a'
a
5. mm Mn Ka 15. kV

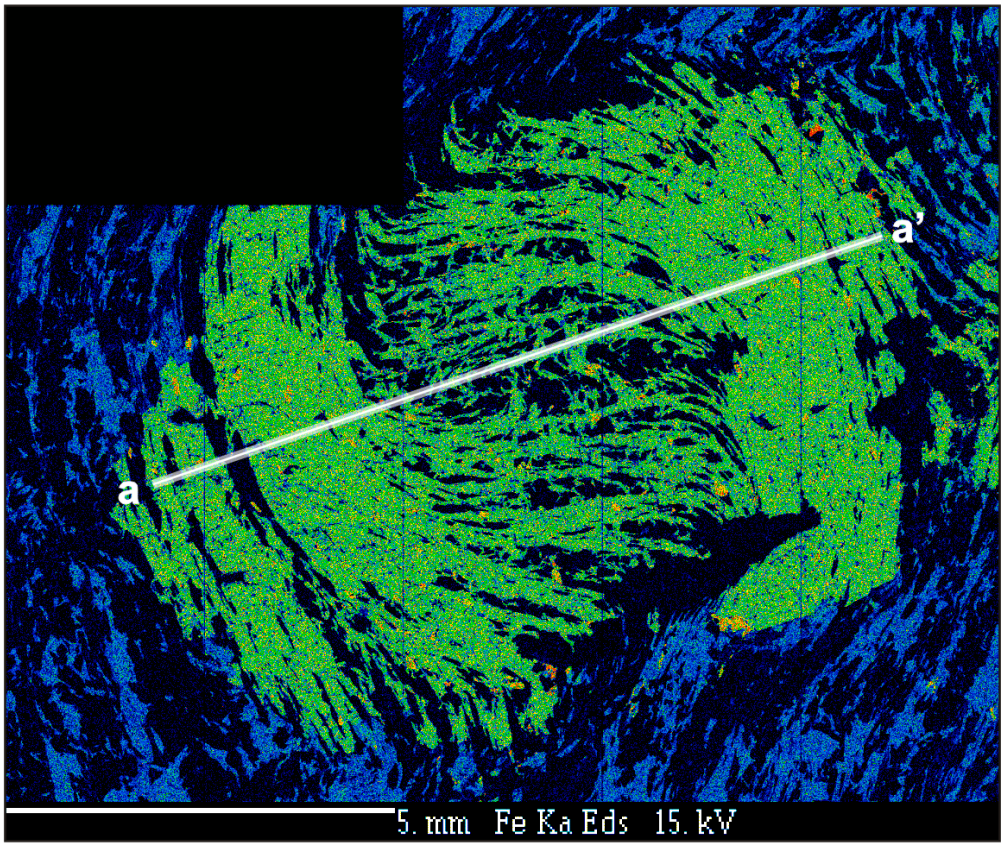
a'
a
5. mm Fe Ka Eds 15. kV

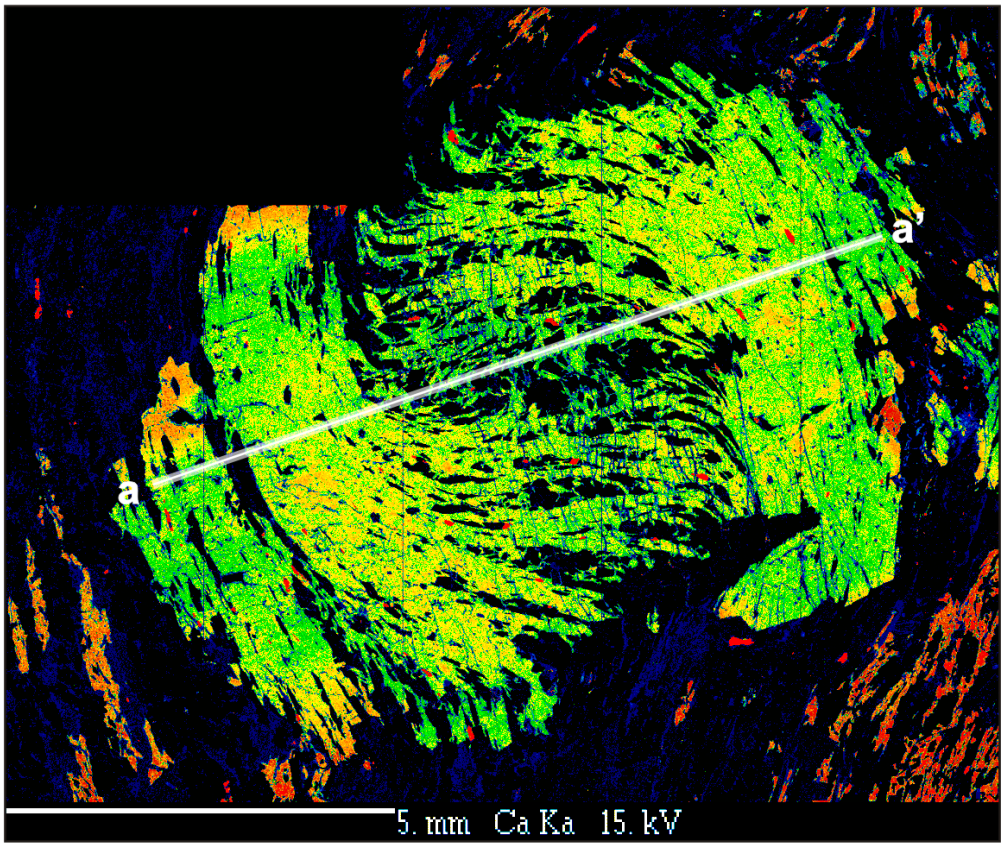
a'
a
5. mm Ca Ka 15. kV

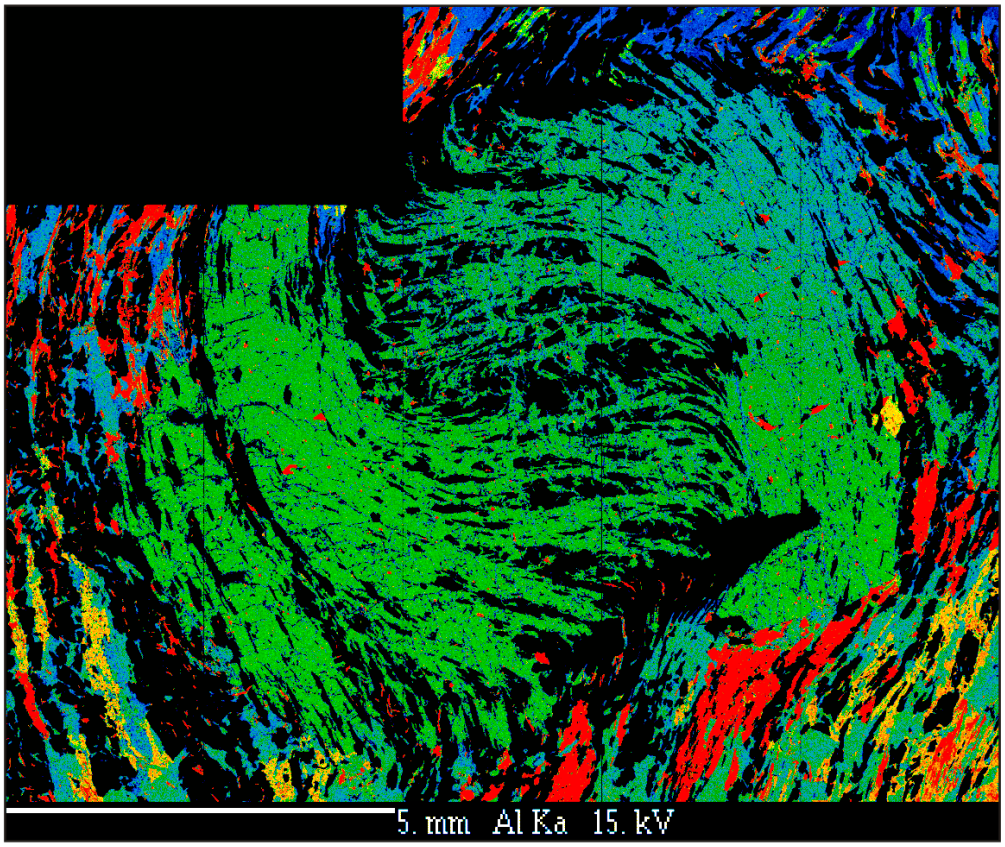
5. mm Al Ka 15. kV

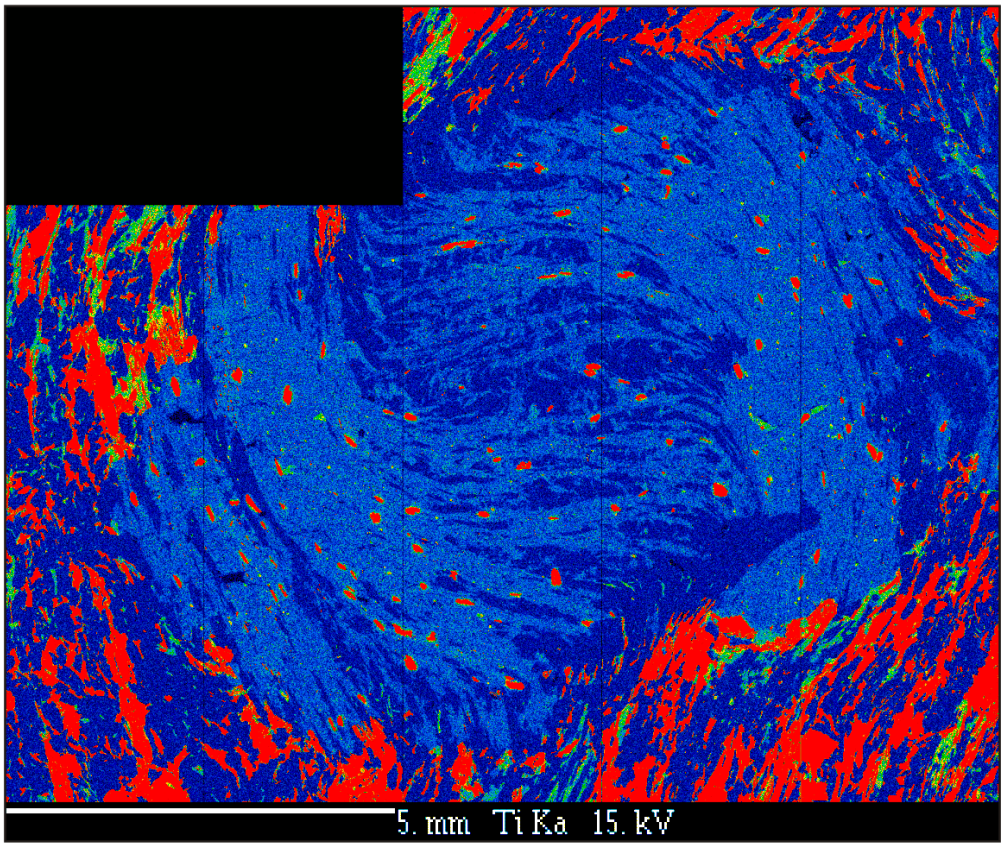
5. mm Ti Ka 15. kV

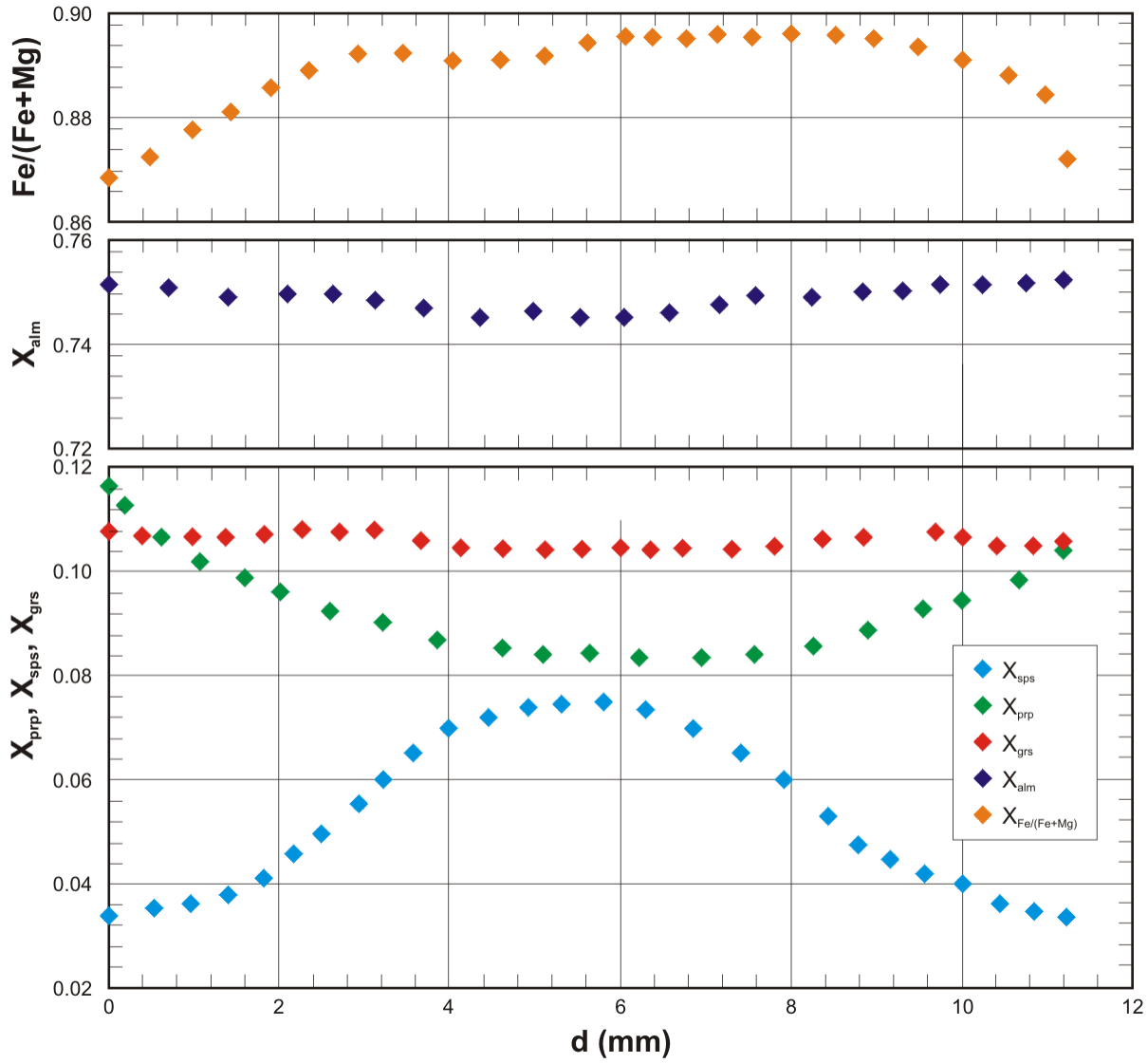

Figure 5. Garnet compositional profiles of X_{alm}, X_{sps}, X_{grs}, X_{alm} and Fe/(Fe+Mg) for sample TM783 (a = 0). Line traverse shown in Figure 4. Note the increase in X_{prp} and the decrease in X_{sps} from core to rim.

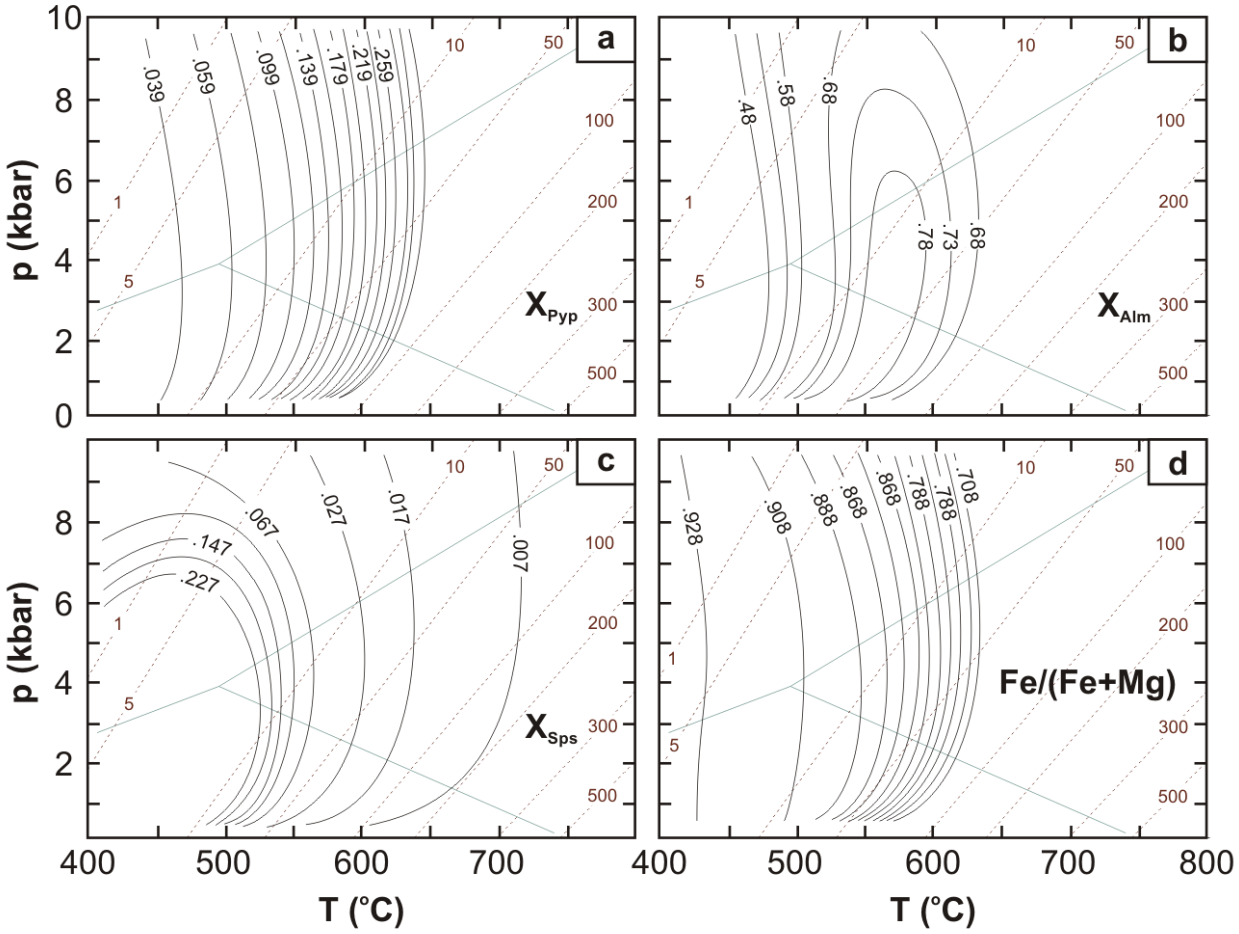

Figure 6. Contours of garnet composition for X_{Pyp}, X_{Alm}, X_{Sps} and Fe/(Fe+Mg) for the garnet + biotite + chlorite + plagioclase + muscovite + quartz in the system MnNCKFMASH. Ti-in-quartz isopleths (red, dashed lines; after Thomas *et al.*, *2010*) and Al_2SiO_5 stability fields (green lines; after Holdaway, 1971) are shown. Isopleths are calibrated to a fixed TiO_2 activity of 1. From Spear *et al.* (1990).

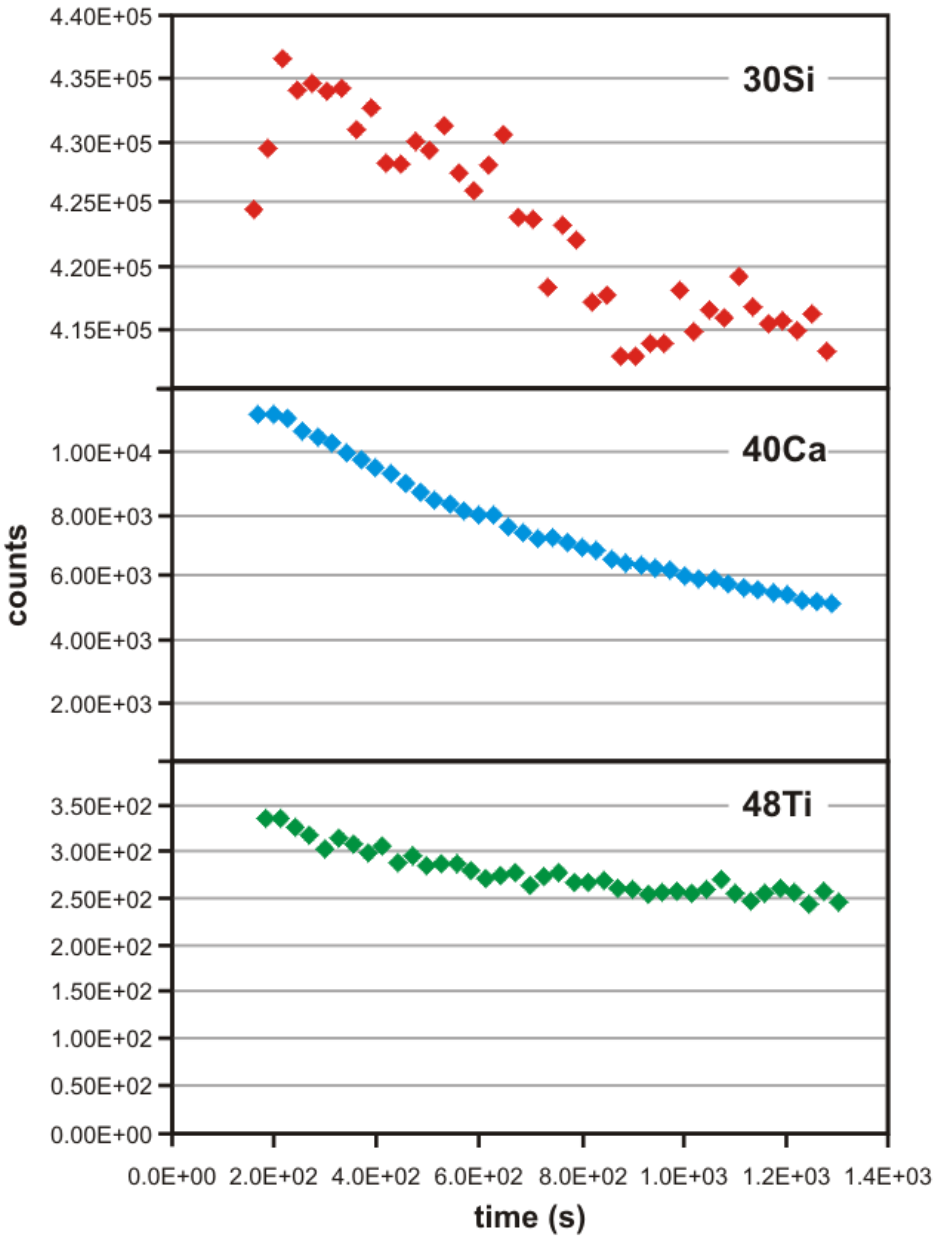

Figure 7. Plots of ^{30}Si, ^{40}Ca and ^{48}Ti counts over time on a quartz inclusion from sample TM783. Surface contamination (presumably due to the gold-coating process) contributes to higher intensities of Ti initially. Measurement of the sample with depth allows for the removal of surface contamination and the data stabilizes at the concentration of Ti in the quartz grain. ^{40}Ca must be measured to subtract the amount of ^{48}Ca interference at mass 48.

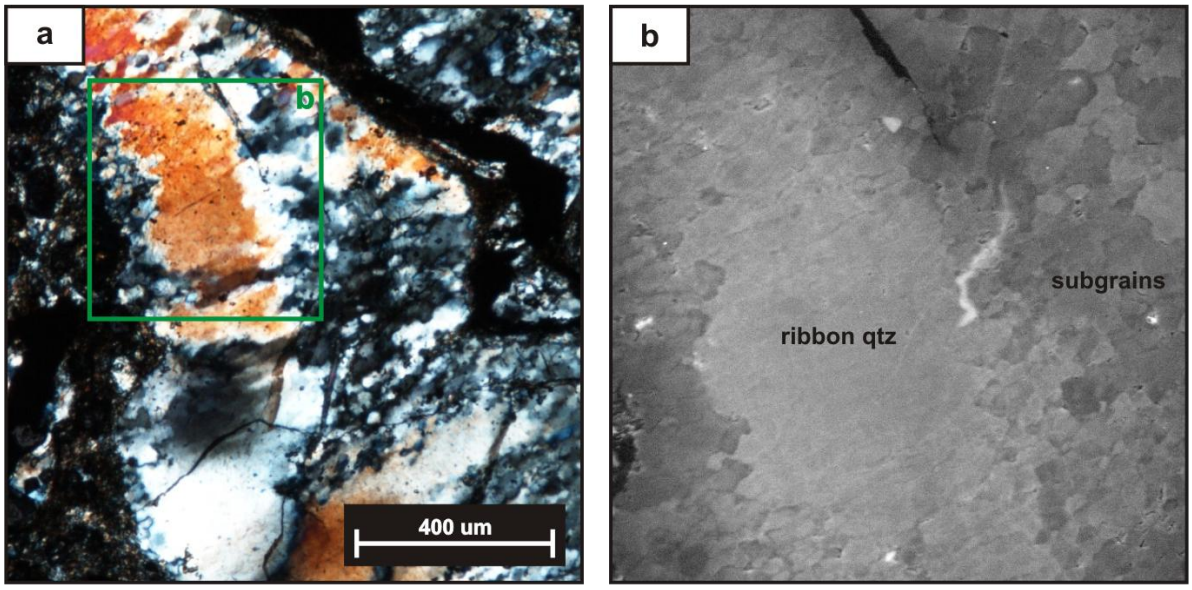

Figure 8. Folded quartz vein from sample TM455. The vein contains ribbon quartz with surrounding newly-formed subgrains (subgrain rotation recrystallization). a) Cross-polarized photomicrograph and b) CL image.

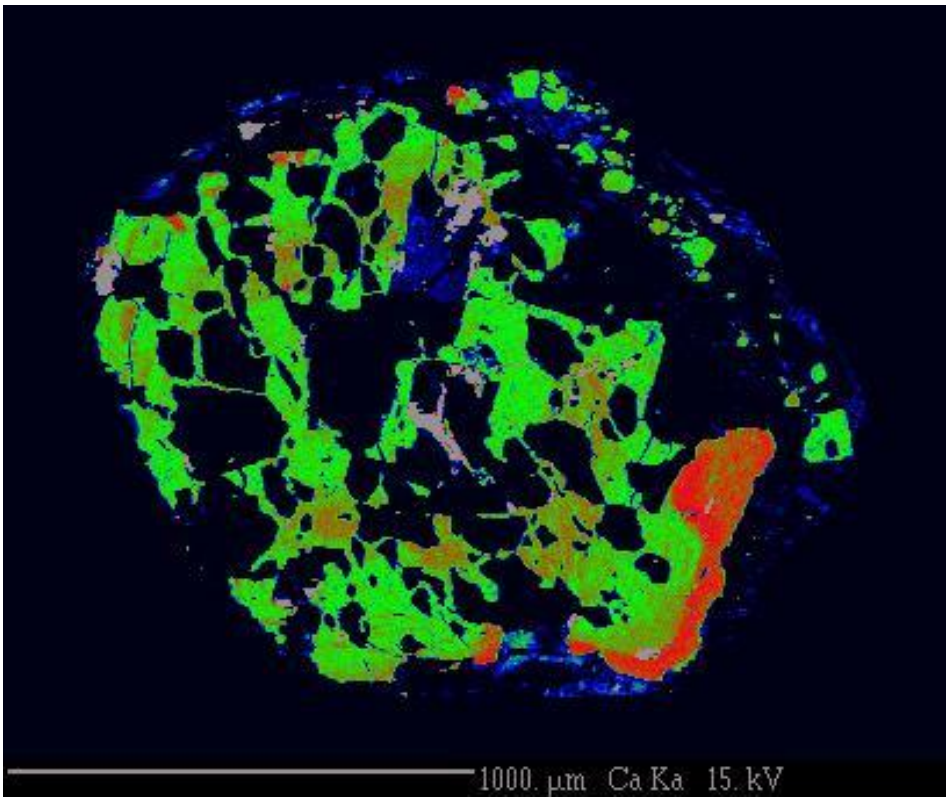

Figure 9. Elemental map of Ca in garnet (sample TM455). Note the significant chemical change (and sharp contact of transition) in lower-right quadrant of the porphyroblast. This is a secondary generation of garnet growth on the original porphyroclast.

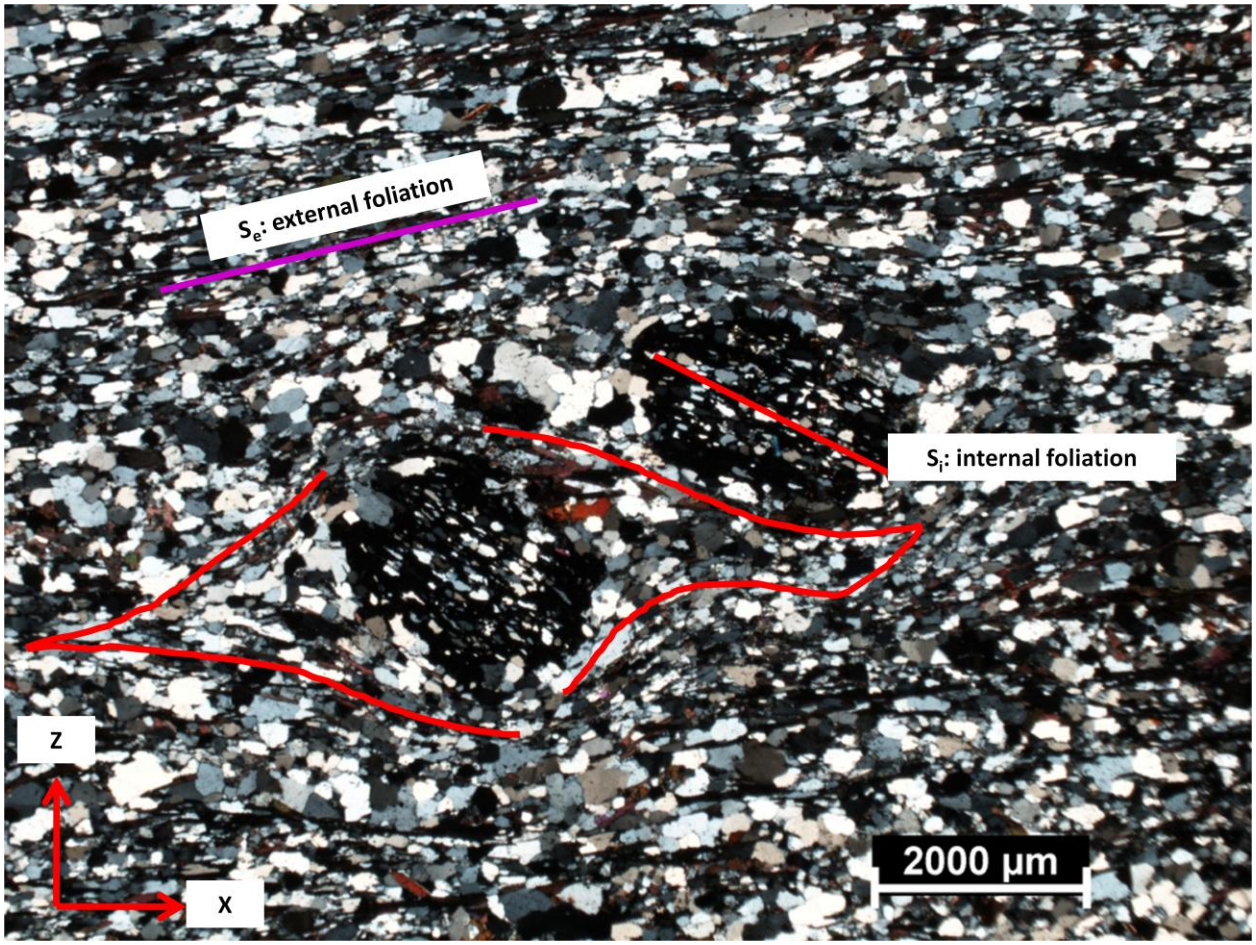

Figure 10. Photomicrograph of sample 09SD08A in cross-polarized light. Garnet porphyroblasts have linear inclusion trails of S_1 that are rotated relative to the external foliation at an oblique angle. Pressure shadows developed in response to inhomogeneous strain (due to the rigidity of the garnet porphyroblasts) applied to the sample. X-direction of cut in is the down-dip direction.

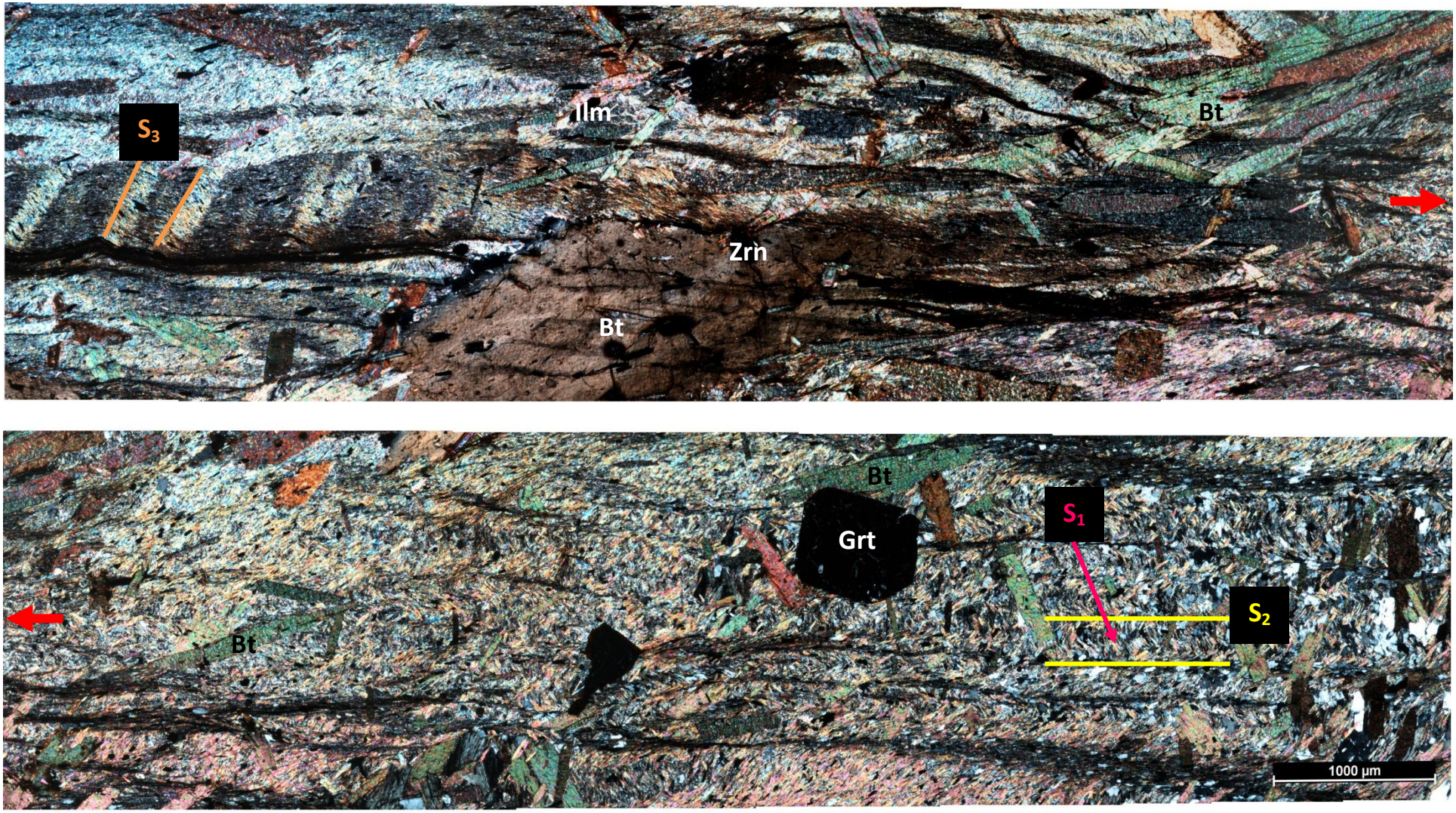

Figure 11. Panorama photomicrograph along the length of the thin section for sample TM623 (may be non-oriented; XPL). A transition from right to left across the photomicrograph shows graded bedding (S_0) with fining left (from coarse quartz to mica). A bedding parallel (S_1) slaty cleavage is defined by mica, which has been crenulated during the D_2 deformation event. In the mica-rich domain to the left, a secondary crenulation cleavage (S_3) is seen contained within the microlithon defined by S_2. Large biotite porphyroblasts with random orientation to foliation are from retrograde metamorphism. Abbreviations from Kretz (1983).